Check for updates

Advanced Engineering Materials

ADVANCED ENGINEERING MATERIALS
www.aem-journal.com

RESEARCH ARTICLE OPEN ACCESS

External and Internal Cracking Caused by Heat Treatment in Laser Powder Bed Fusion-Fabricated Inconel 738LC Components

Kosuke Kuwabara | Masahiro Kusano | Ayako Ikeda | Toshio Osada | Makoto Watanabe

Research Center for Structural Materials, National Institute for Materials Science, Tsukuba, Ibaraki, Japan

Correspondence: Kosuke Kuwabara (kuwabara.kosuke@nims.go.jp)

Received: 10 December 2025 | **Revised:** 21 June 2026 | **Accepted:** 24 June 2026

Keywords: crack | grain boundaries | heat treatment | inconel 738LC | laser powder bed fusion | nickel | superalloy

ABSTRACT

Heat treatment-induced cracking in laser powder bed fusion (LPBF)-fabricated components of a nickel-based superalloy, Inconel 738LC, is systematically investigated under various heat-treatment conditions. Metal additive manufacturing of heat-resistant nickel-based superalloys is a key manufacturing technology for advancing heat engines in aerospace propulsion systems and industrial machinery. In this study, cracks in LPBF-fabricated Inconel 738LC components are characterized after heat treatment at 873–1513 K. The observed cracks are classified into two groups. One group comprises external cracks along high-angle grain boundaries between columnar grains, originating from the bottom or top surfaces. These external cracks begin to propagate during the heating stage at around 1023 K. The other group consists of internal cracks that initiate at flaws such as gas pores and solidification cracks formed during the LPBF rapid solidification process. Heat-treatment conditions are found to influence internal cracking through stress relaxation, strain induced by precipitation, and liquation cracking along grain boundaries. Microstructures after heat treatment are characterized by $L1_2$ (γ') intermetallic precipitates dispersed in a face-centered cubic (γ) matrix and grain boundary carbides, including chromium-rich $M_{23}C_6$ carbides and titanium-rich MC carbides. Finally, crack-free heat-treated LPBF components are fabricated using a modified LPBF laser scan strategy.

1 | Introduction

Metal additive manufacturing (AM) is increasingly recognized as a key manufacturing technology for high-value components [1–3]. The widely recognized advantages of AM over conventional production methods include extended design freedom and direct manufacturing from digital design data. Heat engines in aerospace propulsion systems and industrial machinery are representative AM applications that benefit greatly from these merits because of their ongoing demand for improved performance and reduced environmental impact [2, 4, 5]. Heat-resistant alloys suitable for high-temperature operating environments are one of the major AM material categories developed for the components used in these heat engines. Weldable nickel-based alloys such as Inconel 625 and Inconel 718 have been developed as standard heat-resistant alloys for AM, and they have contributed to the commercialization of heat engines incorporating AM parts [6, 7]. However, heat-resistant AM alloys capable of operating at higher temperature are essential to enable further advances in hot-section components in cutting-edge heat engines.

Heat-resistant nickel-based superalloys are key materials in modern heat engines [8–13]. Their excellent high-temperature mechanical properties and environmental durability enable higher operating temperature of hot sections in heat engines and thereby improve their performance. The excellent high-temperature mechanical properties of nickel-based superalloys originate from precipitation strengthening by intermetallic $L1_2$ (γ') precipitates

This is an open access article under the terms of the Creative Commons Attribution-NonCommercial-NoDerivs License, which permits use and distribution in any medium, provided the original work is properly cited, the use is non-commercial and no modifications or adaptations are made.

© 2026 The Author(s). *Advanced Engineering Materials* published by Wiley-VCH GmbH.

coherently dispersed in a face-centered cubic (γ) matrix. Modern heat-resistant cast nickel-based alloys, including Inconel 738LC, are designed to form higher volume fractions of γ′ precipitates through increased contents of γ′-forming elements such as aluminum and titanium. However, such high γ′-forming element contents tend to cause problems during manufacturing.

Particularly in metal AM processes—for example, laser powder bed fusion (LPBF), electron beam powder bed fusion, and laser directed energy deposition—nickel-based superalloys with higher contents of γ′-forming elements, categorized as nonweldable nickel-based alloys, are prone to cracking [14–19]. Hot cracking, including solidification cracking and liquation cracking, originates from the behavior of residual liquid at grain boundaries between columnar grains. Tensile stresses induced by thermal shrinkage and dynamic γ′ precipitation cause strain-induced cracking [20–22]. Preferential crack propagation along grain boundaries at high temperatures leads to ductility-dip cracking [18, 23]. Cracking during AM of nonweldable nickel-based superalloys is further complicated by the overlapping effects of these different mechanisms.

To overcome the cracking issues in the AM process of nonweldable nickel-based superalloys, alloy development and process development are being actively pursued. Alloy development mainly focuses on the solidification phenomenon to reduce the temperature drop during solidification without deteriorating high temperature mechanical properties [24–28]. Process development is also conducted to control the solidification phenomenon by powder bed preheating, heat source profile arrangement, and melting parameter optimization, including scan strategy investigation in AM processes [29–31]. Process modifications that alter solidification during AM have reduced cracking in some nonweldable nickel-based superalloys; however, postprocessing, especially heat treatment, remains a key factor.

Heat treatment processes of nickel-based superalloys obtained by AM processes are categorized into two groups. One is the hot isostatic pressing process to close the flaws originating in AM processes [32–34]. And the other is the solution and aging heat treatments to modify the physical properties of the product by controlling the crystal grain structures and the precipitation behaviors of γ′ and carbides [35–38]. Cracking in the solution and aging heat treatment processes are also problematic for nickel-based superalloys [39–42]. Miao et al. discussed the liquation cracking by comparing the remelted product with a product after high-temperature heat treatment simulating the heat-affected zone in the remelting process [40]. Safizadeh et al. investigated the cracking of Inconel 738LC LPBF components during heat treatment and proposed a simulation process to predict crack locations [41]. Former studies mainly investigated the influence of the standard solution heat treatment and aging heat treatment developed for the cast products. However, the influence of the heat treatment conditions on the cracking behaviors and resultant microstructures for AM products have not been fully systematically investigated.

In this study, heat treatment conditions for a nonweldable nickel-based superalloy fabricated by LPBF were systematically investigated to unveil the cracking mechanisms during heat treatment. The nickel-based superalloy Inconel 738LC was selected owing to its proven high-temperature durability in cast components and its potential as a next-generation heat-resistant alloy for AM. The dependence of crack distribution and microstructure on heat-treatment temperature and duration was examined. This study covers wide range of temperatures at which various heat treatments have traditionally been performed, with the aim of elucidating the potential effects of these specific heat treatments on cracking. Two types of LPBF-fabricated components with different initial microstructures were used to elucidate the influence of the as-built microstructure on that obtained after heat treatment.

2 | Results

2.1 | Phase Constitutions and Crack Distributions

X-ray diffraction (XRD) measurements were conducted for LPBF components obtained with scan strategy A before and after heat treatment to identify the basic material systems of the products in this study (Figure 1). The XRD spectra confirmed that the matrix phase of all specimens was based on γ phase. The variation in the peak height ratios among specimens was due to differences in the sampling orientation. Independent peaks from γ′ precipitates were not detected, which indicated that all peaks originated from γ matrix and γ′ precipitates overlapped with each other. No notable minor peaks originating in other phases, including carbides, were identified in heat-treated specimens, possibly due to their smaller volumetric fractions.

Crack distributions in LPBF components before and after heat treatment were imaged by observing vertical cross sections of the cylinder specimens using a digital microscope (Figure 2). The as-built specimen obtained with scan strategy A contained massive short cracks no more than 0.2 mm in length, which appeared as bright straight lines in the micrographs. Most of the cracks aligned along building directions. All heat-treated specimens contained long cracks initiated from bottom or top surfaces. These long cracks reached more than 1 mm in depth and extended along building directions. In this study, these long cracks were defined as “external cracks” because, as will be shown in the following section, they always originate at the surface areas and propagate inward. Short cracks other than external cracks were defined as “internal cracks” because, unlike external cracks, they originate from flaws within the specimen. In the range below 1200 K, the depth of the external cracks increased as the heat treatment temperature rose, but no clear relationship was observed in the higher temperature range (Figure S3). All specimens obtained with scan strategy B showed a few internal cracks in the bottom areas close to the support structures, as was previously reported for as-built specimens [43]. External cracks were identified in the heat-treated specimens obtained with scan strategy B, but these cracks were not as deep as those in the specimens obtained using scan strategy A.

2.2 | External Crack Tip Characterization

The tips of external cracks in heat-treated specimens were characterized by scanning electron microscopy (SEM) to investigate propagation morphologies (Figure 3). The external cracks

15272648, 2026, 18, Downloaded from https://advanced.onlinelibrary.wiley.com/doi/10.1002/adem.71079 by National Institute For, Wiley Online Library on [22/09/2026]. See the Terms and Conditions (https://onlinelibrary.wiley.com/terms-and-conditions) on Wiley Online Library for rules of use; OA articles are governed by the applicable Creative Commons License

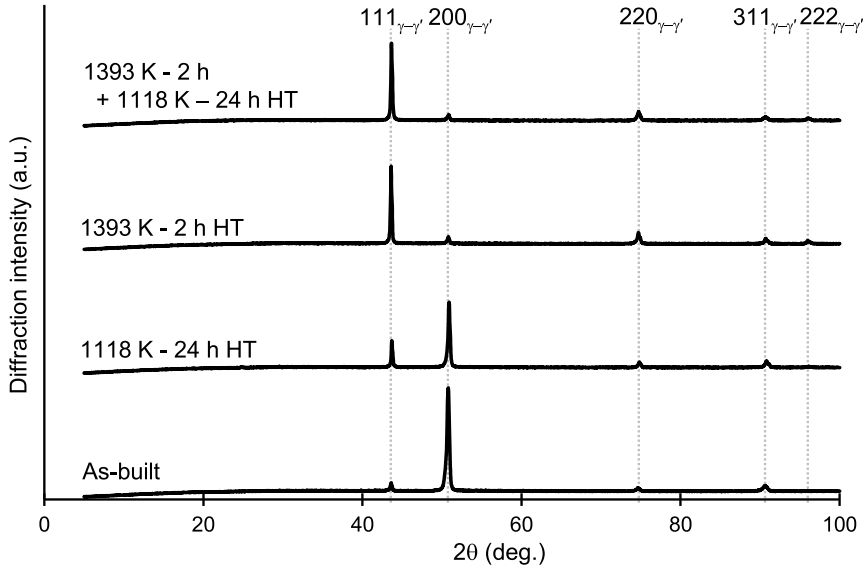


FIGURE 1 | XRD spectra obtained from as-built and heat-treated specimens.

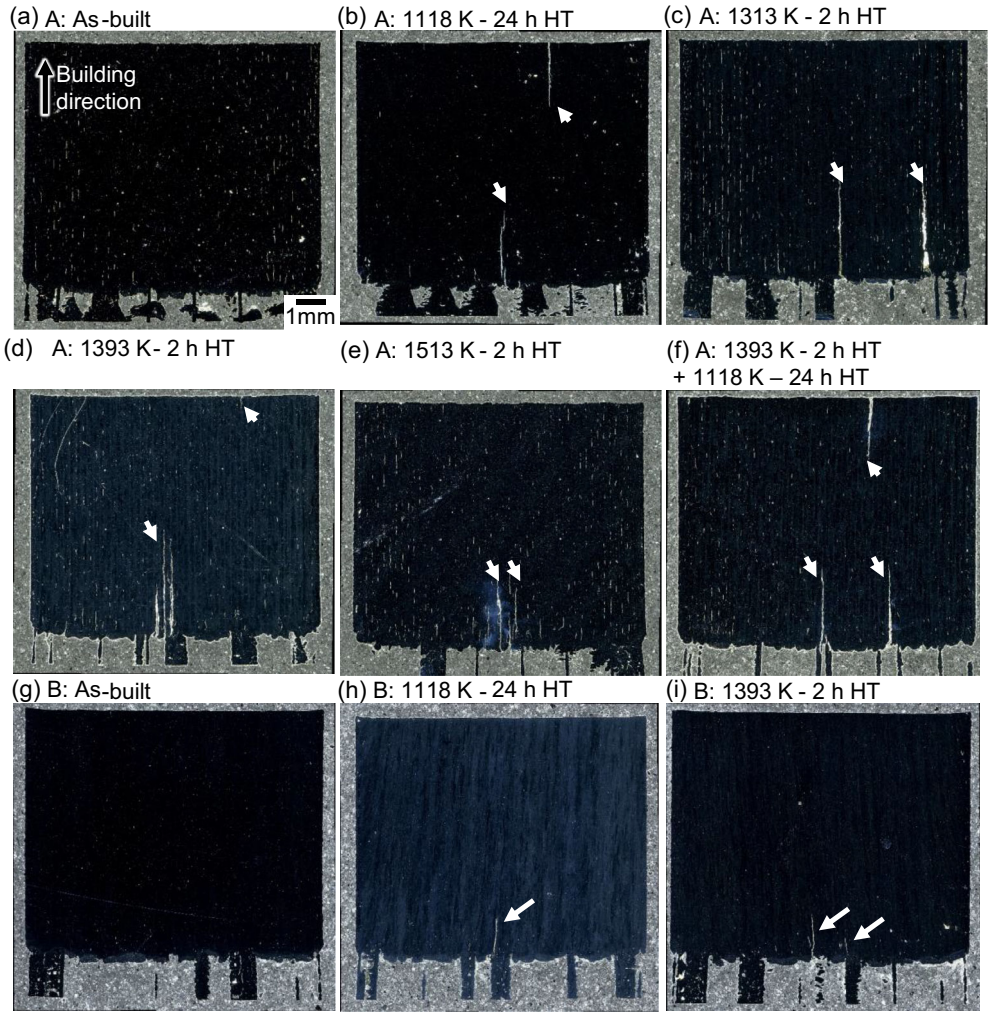


FIGURE 2 | (a–i) Cross sections of the LPBF specimens obtained with scan strategies A and B observed with a digital microscope. Scan strategies and heat treatment conditions are shown with labels. Arrows indicate external cracks.

15272648, 2026, 18, Downloaded from https://advanced.onlinelibrary.wiley.com/doi/10.1002/adem.71079 by National Institute For, Wiley Online Library on [22/09/2026]. See the Terms and Conditions (https://onlinelibrary.wiley.com/terms-and-conditions) on Wiley Online Library for rules of use; OA articles are governed by the applicable Creative Commons License

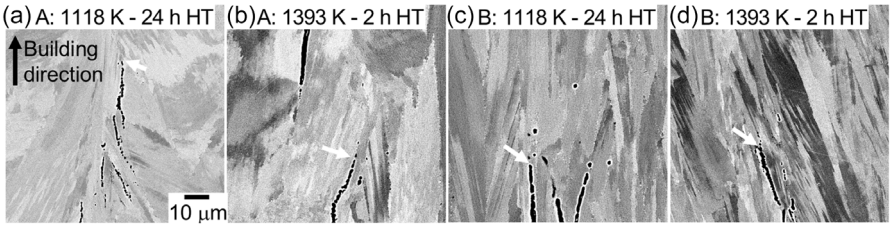


FIGURE 3 | (a–d) External cracks in heat-treated specimens obtained with scan strategies A and B. Scan strategies and heat treatment conditions are shown with labels. Arrows indicate the tips of the external cracks.

extended along grain boundaries by linking the short individual cracks together. Consecutive micropores along grain boundaries were identified in the extension of the crack tips. The cracks appeared to proceed by repeatedly forming and integrating micropores at the crack tips. All heat-treated specimens processed at ≥1118 K, including those obtained with scan strategy B, exhibited external cracks with the same characteristic morphologies. Electron probe microanalysis (EPMA) (Figure 4) revealed that the surface of the external crack was coated by the bilayer oxide film. The outer layer was mainly composed of aluminum and titanium oxide, while the inner layer was chromium oxide film. Aluminum and titanium were deficient in the inner layer. These oxide-forming elements were deficient in the small cracks and micropores formed along the grain boundaries in the extension of the external crack tip.

2.3 | Propagation of External Cracks

To understand the driving force behind the external cracking, residual stresses were measured in the center of the top surfaces of LPBF cylinder-shaped products (Figure 5a) by the XRD method. Residual stresses close to the yield stress (900 MPa at room temperature [44]) were detected in as-built specimens.

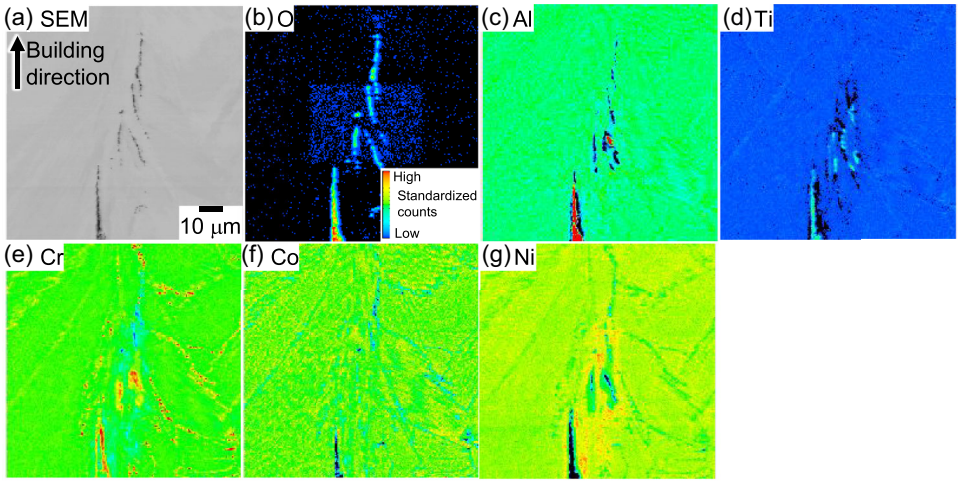


FIGURE 4 | Qualitative elemental distributions around external crack tips in a specimen produced with scan strategy A after 24 h heat treatment at 1118 K obtained by EPMA. (a) SEM image (b–g) elemental distribution.

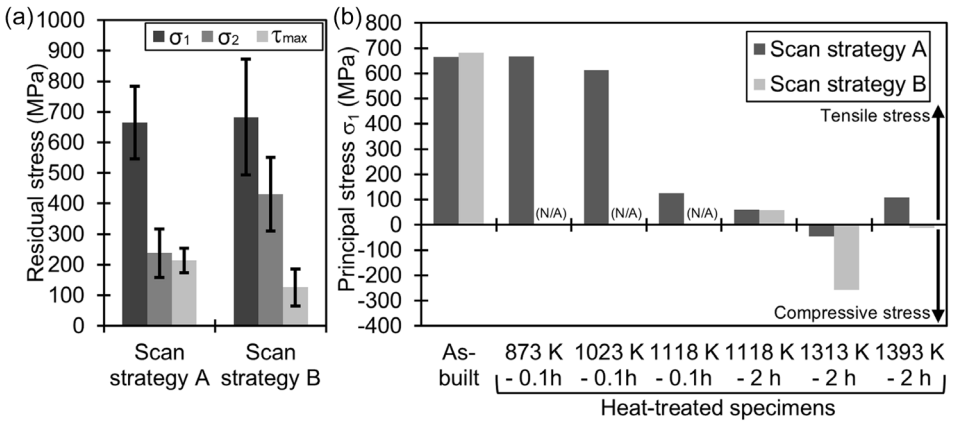


FIGURE 5 | (a) Residual stress of as-built specimens produced with scan strategy A and B. Error bars indicate standard deviations. (b) Residual stress (σ_1) of specimens before and after heat treatment.

15272648, 2026, 18, Downloaded from https://advanced.onlinelibrary.wiley.com/doi/10.1002/adem.71079 by National Institute For, Wiley Online Library on [22/09/2026]. See the Terms and Conditions (https://onlinelibrary.wiley.com/terms-and-conditions) on Wiley Online Library for rules of use; OA articles are governed by the applicable Creative Commons License

Scan strategy A specimens exhibited anisotropic residual stresses, with the maximum principal stress (σ_1) oriented along the scan direction in the top layer. The residual stress anisotropy in scan strategy B specimens was less significant, though the stress amplitudes were comparable to those of scan strategy A specimens.

The values of the maximum principal residual stress σ_1 for the heat-treated specimens are summarized in Figure 5b. Scan strategy A specimens were heat-treated for a shorter duration (0.1 h) to reproduce the specimens during the heating-up step in the heat treatment. Residual stress significantly decreased after 0.1 h of heat treatment at 1118 K. Cracks perpendicular to the laser scan direction were identified on the top surface (Figure 6c,d). External cracks from the bottom surface were also identified in the cross section of the specimen heated to 1023 K (Figure 6b).

Figure 7 shows the microstructure around the external crack tip reflecting the early-stage external cracks in the specimen heat-treated at 1023 K for 0.1 h, as observed using EPMA and electron backscattering diffraction (EBSD). Consecutive micropores were not found in the extension of the crack tip, unlike in the specimens treated at higher temperatures (Figures 3 and 4). Surface oxide film was not identified under this condition other than the chromium-deficient layers on the crack surface. The crack propagated along high angle grain boundaries (HAGBs). The crack tip in Figure 7 showed the zig-zag morphology corresponding to a high angle grain boundary between two columnar grains with different growth directions. The microcells in both grains collided with one another, forming grain boundaries with a zig-zag morphology. The crystal strain around the crack tip detected in the Kernel average misorientation (KAM) map

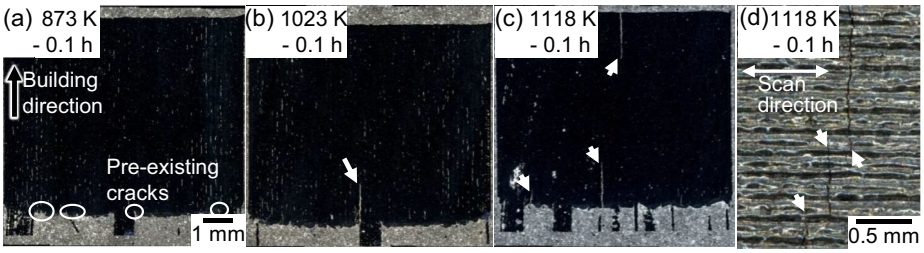


FIGURE 6 | (a–c) Cross sections of scan strategy A specimens after heat treatment for 0.1 h. (d) An external crack observed on the top surface. Arrows indicate external cracks.

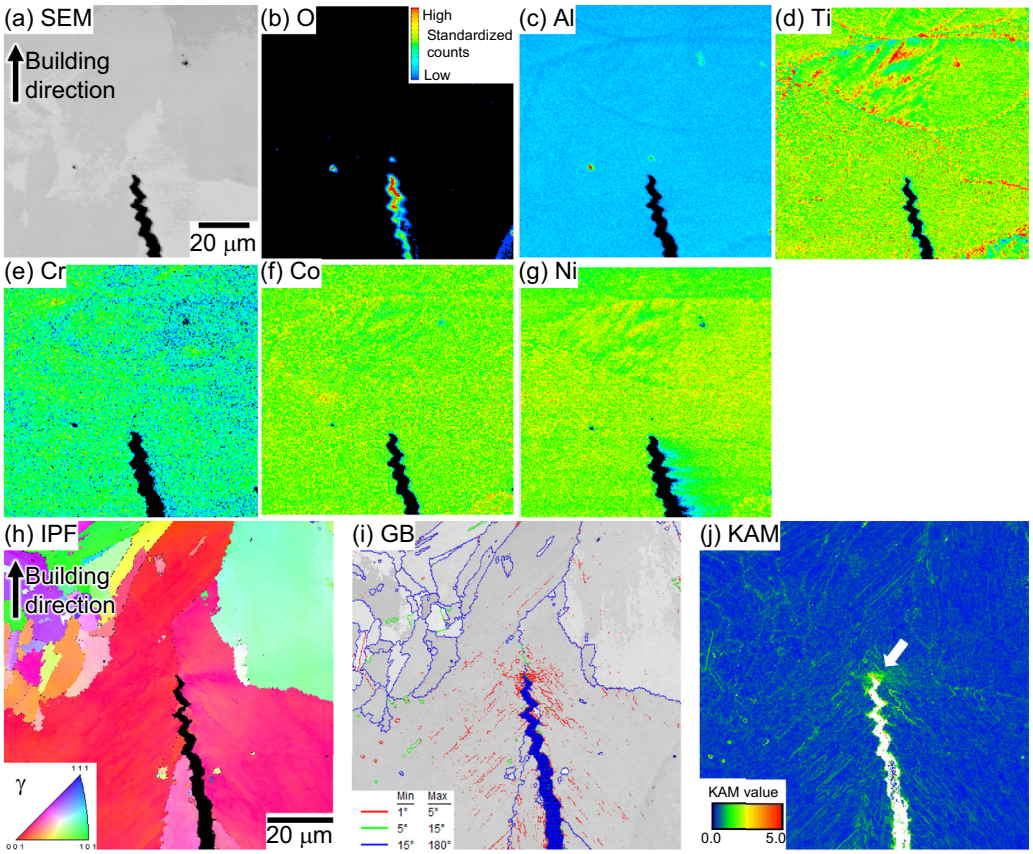


FIGURE 7 | External crack tips in specimens heat-treated at 1023 K for 0.1 h. (a) Microstructure. (b–g) Elemental distributions obtained using an EPMA (h) inverse pole figure (IPF) map relative to the vertical line on the observation plane. (i) Grain boundary map. (j) Kernel average misorientation (KAM) map obtained by electron backscattering diffraction (EBSD).

15272648, 2026, 18, Downloaded from https://advanced.onlinelibrary.wiley.com/doi/10.1002/adem.71079 by National Institute For, Wiley Online Library on [22/09/2026]. See the Terms and Conditions (https://onlinelibrary.wiley.com/terms-and-conditions) on Wiley Online Library for rules of use; OA articles are governed by the applicable Creative Commons License

(Figure 7j) indicated plastic deformation caused by crack propagation during the heating-up step.

2.4 | Microstructure around Internal Cracks and Grain Boundaries

The internal cracks in the digital microscope images in Figure 2 were detected using Image J software [45–49] for statistical analysis (Figure 8). Defects with areas over 50 μm^2 and aspect ratios over 3 detected in the binarized images (Figure 8a–f) were defined as internal cracks in this investigation. Cracks connected to the specimen surfaces were regarded as external cracks and were omitted from the count of internal cracks; however, certain crack chains that were part of an external crack extending from the surface through the specimen inside were still included in the count to avoid the underestimation of the crack density by excluding interconnected internal crack chains illustrated in Figure S5b. Crack length was defined as half the defect's perimeter for simplicity, as shown in the inset of Figure 8g.

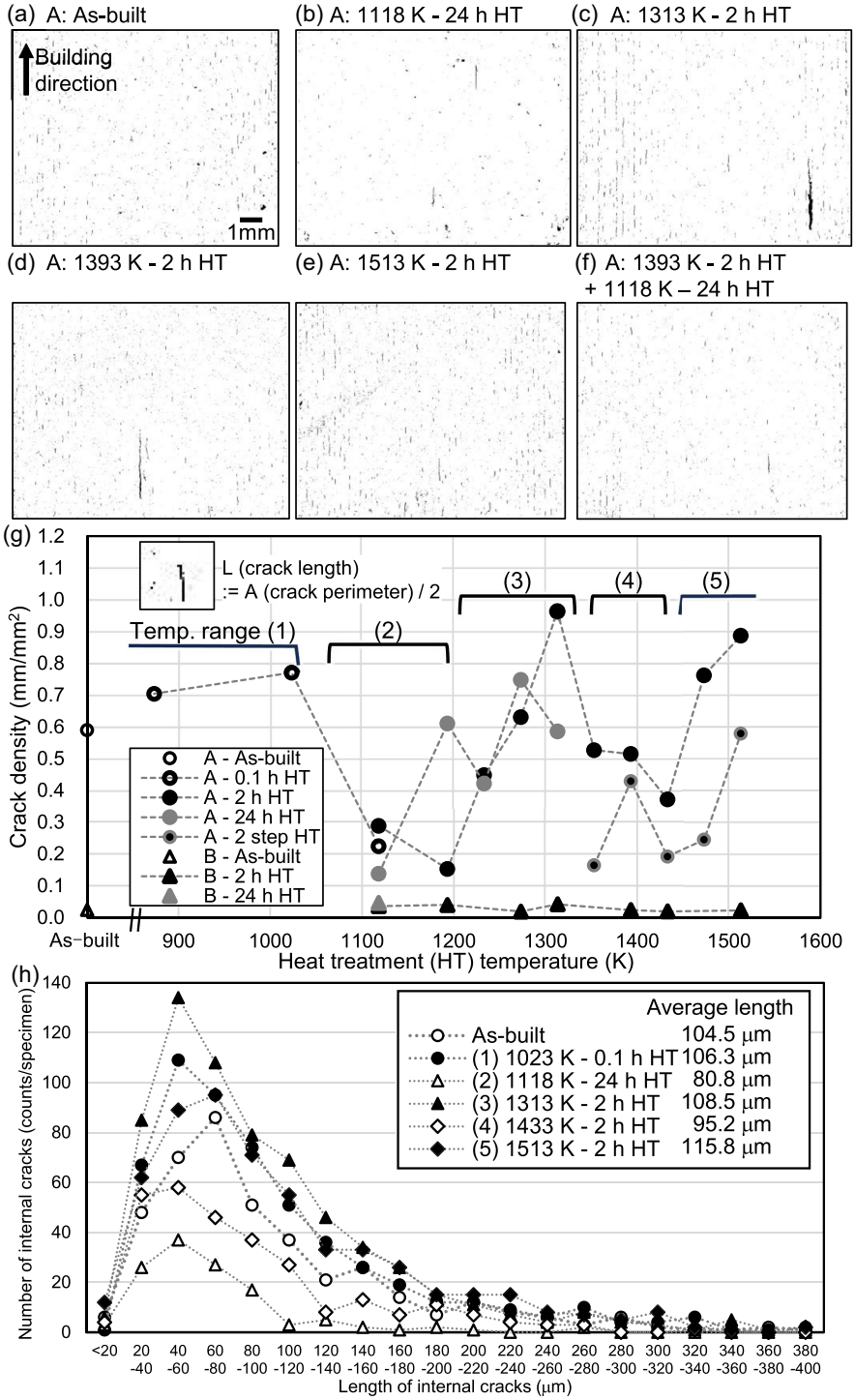


FIGURE 8 | (a–f) Internal cracks detected in the binarized images. (g) Density of internal cracks detected in LPBF components after heat treatment. (h) Internal crack-length histograms of selected components in (g).

15272648, 2026, 18, Downloaded from https://advanced.onlinelibrary.wiley.com/doi/10.1002/adem.71079 by National Institute For, Wiley Online Library on [22/09/2026]. See the Terms and Conditions (https://onlinelibrary.wiley.com/terms-and-conditions) on Wiley Online Library for rules of use; OA articles are governed by the applicable Creative Commons License

The internal crack densities in all heat-treated specimens (Figure 8g) exhibited three peak temperature ranges: a lower temperature range below 1100 K (range 1), an intermediate temperature range of 1233–1313 K (range 3), and a high temperature range over 1473 K (range 5). Heat treatment in the temperature range of 1118–1193 K (range 2) reduced internal cracks for all of three specimens heat-treated at 1118 K and a specimen heat-treated at 1193 K for 2 h. A two-step heat treatment ending with an aging treatment at 1118 K for 24 h suppressed the formation of internal cracks to the same extent as a one-step heat treatment at 1118 K for 24 h. The crack density in the as-built specimen obtained with scan strategy B was less than one-tenth of that in the corresponding specimen obtained using scan strategy A. In specimens fabricated with scan strategy B, the crack density was essentially independent of the heat treatment conditions.

Crack length histogram of selected specimens belonging to temperature ranges 1–5 (Figure 8h) indicated that low-temperature heat treatment (range 2) effectively reduced the number of longer cracks over 100 μm. It seemed that residual stress relief caused by 1118–1193 K heat treatment inhibited the further crack propagation from flaws in as-built specimens and caused the crack gap to close, resulting in the reduced crack length observed in the cross-section analysis. Higher numbers of cracks were detected in all bins after heat treatment at lower (range 1) and higher (range 3) temperature ranges. Compared to the other temperature ranges, heat treatment at still higher temperatures (range 5) yielded more internal cracks longer than 140 μm. The average lengths of crack length after heat treatments were reflected by these changes in the distributions.

The internal cracks in LPBF components before and after heat treatment were characterized by scanning electron microscope (SEM) (Figure 9) and EBSD (Figure 10) to characterize the microscopic features around them. They were preferentially located along HAGBs. Most cracks exhibited the typical morphologies of solidification cracks characterized by the repeated bumps and dendrite structures. Some cracks with no bumps seemed to be formed by the propagation of the cracks along HAGBs from the solidification cracks and gas pores trapped along grain boundaries. The crystal strain field around these nonsolidification crack tips in KAM maps (Figure 10(a3)(b3)(c3)) implied the crack propagation after heat treatment because no microstructural evolution corresponding to the strain field was observed.

Grain boundary microstructures were observed at a higher magnification to evaluate the distributions of precipitates in LPBF specimens. The micrographs of specimens obtained with scan strategy A are summarized in Figure 11, since it was found that the scan strategy did not affect the distributions of precipitates. Columnar grains in the as-built specimen contained microcellular structures. No intermetallic precipitates were identified other than fine MC carbides rich in titanium preferentially distributed in the boundary areas of microcells. In heat-treated specimens, the microcells were diminished and fine γ' precipitates formed in columnar grains. Coarse γ' precipitates were found along grain boundaries in the specimens heat-treated at higher temperatures.

The average diameter and areal fraction of γ' precipitates were obtained by image analysis using ImageJ software for specimens in which the γ' precipitates were sufficiently large to be distinguished from the γ matrix in SEM images at magnifications of 30k ($T < 1200$ K) and 10k ($T > 1200$ K) (Figures 12 and S4). The reduction in the areal fraction and the increase of the diameter for higher heat treatment temperatures were confirmed. The specimens heat-treated at higher than 1433 K showed smaller γ' precipitates due to the partial dissolution and reprecipitation during the cooling step. No notable difference in the γ' precipitate distribution was identified for 2-step heat treatment after heat treatment at 1118 K for 24 h.

Other than γ' precipitates, chromium-rich $M_{23}C_6$ carbides and titanium-rich MC carbides precipitated along grain boundaries after heat treatment at lower temperature and higher temperature, respectively. Chromium and titanium preferentially distributed in the grain boundary precipitates in specimens heat-treated at lower and higher temperatures, respectively which were confirmed in scanning electron microscope-energy dispersive X-ray spectroscopy (EDS) elemental mapping shown in Figure S2. The transition temperature from $M_{23}C_6$ to MC carbide was estimated to be around 1273 K, at which less grain boundary carbide precipitates were identified. Voids along grain boundaries were

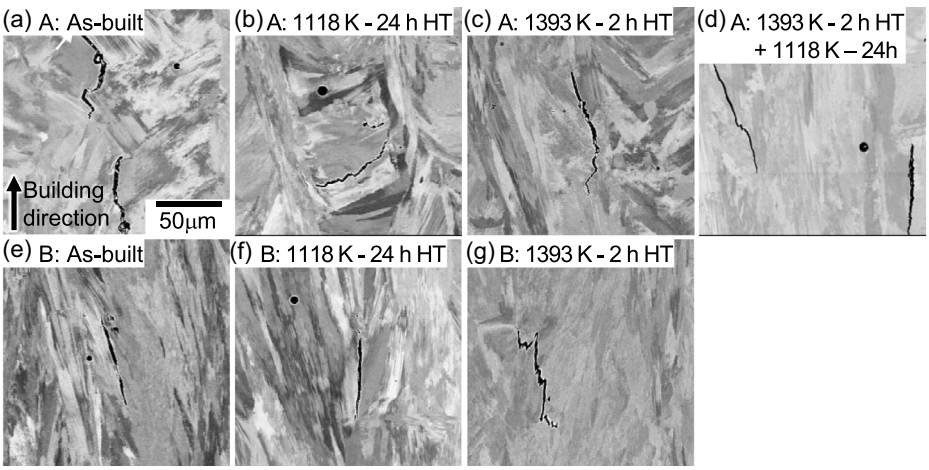


FIGURE 9 | (a–g) Typical internal cracks identified in as-built and heat-treated LPBF components formed with scan strategies A and B. Scan strategies and heat treatment conditions are shown with labels.

15272648, 2026, 18, Downloaded from https://advanced.onlinelibrary.wiley.com/doi/10.1002/adem.71079 by National Institute For, Wiley Online Library on [22/09/2026]. See the Terms and Conditions (https://onlinelibrary.wiley.com/terms-and-conditions) on Wiley Online Library for rules of use; OA articles are governed by the applicable Creative Commons License

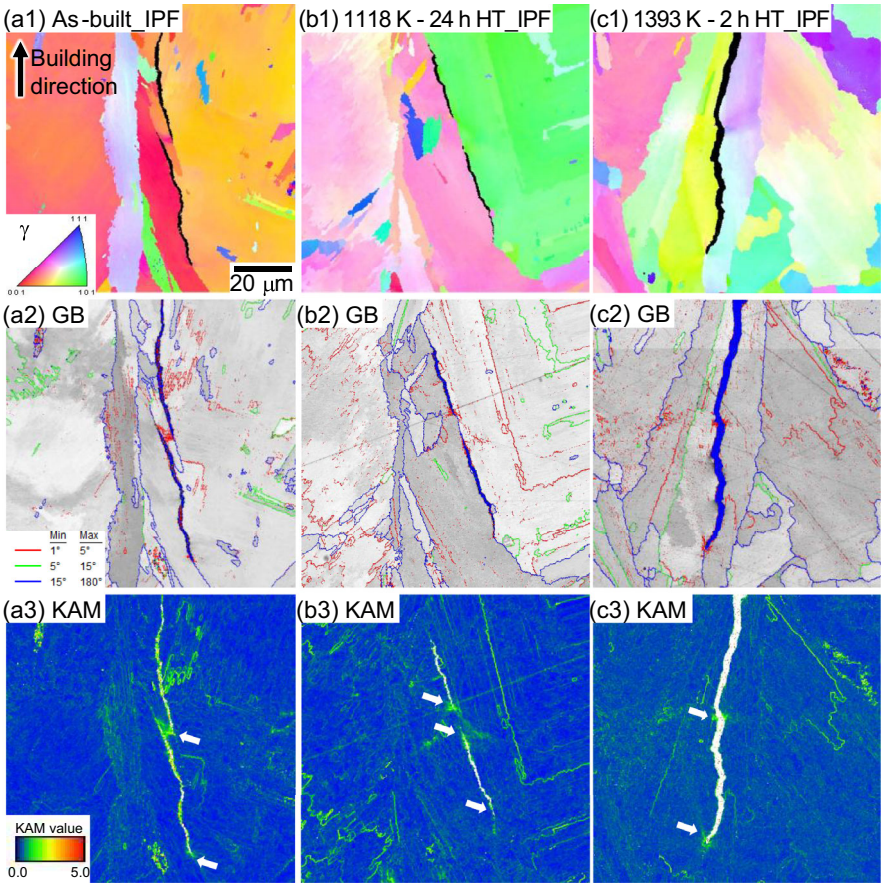


FIGURE 10 | (a1)(b1)(c1) IPF, (a2)(b2)(c2) GB and (a3)(b3)(c3) KAM maps obtained by EBSD around the internal cracks in LPBF components formed with scan strategy A. IPF was plotted relative to the vertical line on the observation plane. Arrows in KAM maps indicate the crystal strain field on the edge of internal cracks.

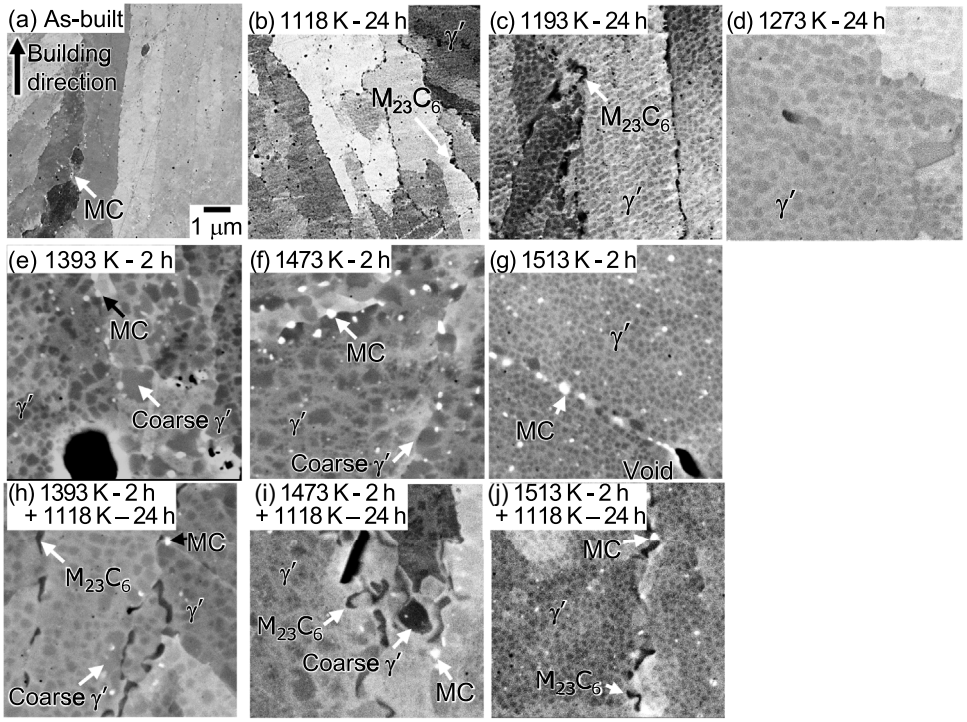


FIGURE 11 | (a–j) Grain boundary microstructures identified in LPBF components formed with scan strategy A. Heat treatment conditions are shown with labels.

15272648, 2026, 18, Downloaded from https://advanced.onlinelibrary.wiley.com/doi/10.1002/adem.71079 by National Institute For, Wiley Online Library on [22/09/2026]. See the Terms and Conditions (https://onlinelibrary.wiley.com/terms-and-conditions) on Wiley Online Library for rules of use; OA articles are governed by the applicable Creative Commons License

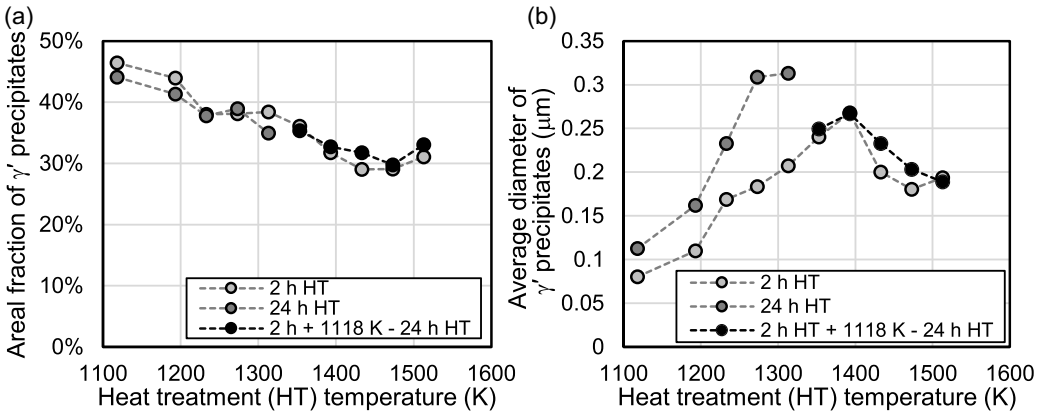


FIGURE 12 | (a) Areal fractions and (b) average diameters of γ′ precipitates obtained by the SEM micrograph image analysis for LPBF components formed with scan strategy A.

identified after heat treatment over 1433 K. LPBF specimens after 2-step heat treatment exhibited relatively coarse $M_{23}C_6$ carbides elongated along grain boundaries.

Micro-Vickers hardness was measured to evaluate γ′ precipitation-strengthening behavior in the LPBF components (Figure 13). All heat-treated specimens exhibited higher hardness than the as-built specimens. Specimens heat-treated at lower temperatures for shorter duration showed higher hardness, suggesting that the heat-treatment conditions investigated in this study lie in the over-aged regime. γ′ precipitation appears to start during the heating-up step, as indicated by the increased hardness in specimens heat-treated for only 0.1 h. LPBF components fabricated with scan strategy B showed no significant difference in hardness from those fabricated with scan strategy A.

3 | Discussion

3.1 | Microstructure Evolution During LPBF and Heat Treatment

Crack analysis of LPBF-fabricated Inconel 738LC components showed that both external and internal cracks formed and propagated along grain boundaries. Thus, a review of the microstructure evolution during LPBF and subsequent heat treatment, which determines the grain-boundary structure, should precede the discussion of cracking behavior.

Figure 14a shows the solid phase fraction during the LPBF solidification process, thermodynamically calculated using a Scheil model with solute trapping (Thermo-Calc 2024a, TCNI12 database) to consider the nonequilibrium rapid solidification process. The temperature interval corresponding to an increase in the solid fraction from 90% to 99% (ΔT) was found to be 107 K. Considering previous work on the printability of nickel-based alloys [25, 28], this ΔT implies a relatively high risk of hot cracking in this alloy. The calculated compositions of the liquid phase during solidification (Figure 14b) indicated the enrichment of Ti, W, Ta, Zr, and B in the liquid. These elements therefore appear to segregate along grain boundaries between columnar grains in LPBF components.

The equilibrium phase fractions based on the bulk composition and on the simulated liquid composition corresponding at a solidification fraction of 0.90 were calculated to estimate the phases forming in grains and along grain boundaries in the heat treatment process, respectively. The phase fraction of γ′ in Figure 14c agreed qualitatively with the observed γ′ areal fraction in Figure 12a, although the calculated γ′ solvus temperature appeared lower. The solidus temperature in Figure 14d was

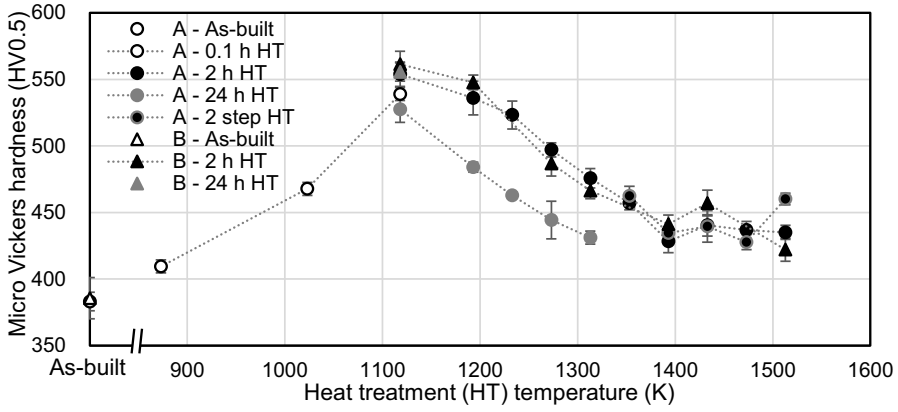


FIGURE 13 | Micro-Vickers hardness of LPBF components formed with scan strategy A and B after heat treatment. Error bars indicate standard deviations.

15272648, 2026, 18, Downloaded from https://advanced.onlinelibrary.wiley.com/doi/10.1002/adem.71079 by National Institute For, Wiley Online Library on [22/09/2026]. See the Terms and Conditions (https://onlinelibrary.wiley.com/terms-and-conditions) on Wiley Online Library for rules of use; OA articles are governed by the applicable Creative Commons License

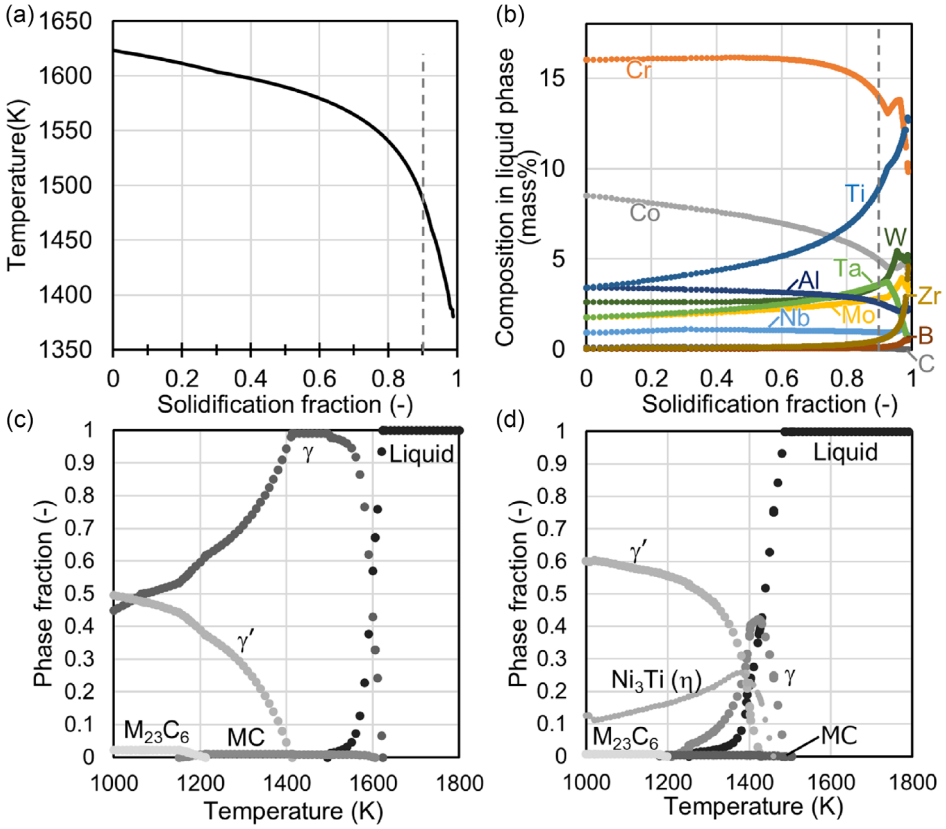


FIGURE 14 | Phase transformation behavior thermodynamically calculated using Thermo-Calc, (a) Temperature drop during solidification. (b) Composition of the liquid phase during solidification. (c) Phase fractions calculated using the bulk composition. (d) Phase fractions calculated using the liquid composition at a solid fraction of 0.90 in (b).

reduced by the γ–γ′ eutectic reaction caused by titanium and tantalum enrichment. These results indicate the possibility of local melting along grain boundary voids, as observed in specimens heat-treated at 1433 K and above. The stable carbide phase changes from chromium-rich $M_{23}C_6$ to titanium-rich MC around 1250 K, which agreed well with the grain-boundary characterization results in Figure 11. No notable changes in the stability of the carbide phases were found in Figure 14c,d.

In the heat treatment of Inconel 738LC LPBF components, γ′ and carbide precipitate in parallel to form the typical microstructure of nickel-based superalloys, γ matrix with dispersed γ′ precipitates and grain boundaries pinned with carbide precipitates. $M_{23}C_6$ carbide forms at lower temperatures, and MC carbide forms at higher temperatures. The morphologies and the volume of precipitates depend on both temperature and duration of the heat treatment. Residual stress would be released as the as-built microstructure transforms, however γ′ precipitation induces additional strains [46]. Partial melting around grain boundaries resulting in liquation cracking possibly occurs over 1433 K.

3.2 | Mechanism of External Cracking

External cracking occurred in all heat-treated LPBF specimens. Key findings about external cracking are listed below.

- Cracks initiate from the bottom or the top surfaces of the specimen.
- External cracks in specimens obtained with LPBF scan strategy B are shorter, and they initiated from bottom surface only.
- Cracks start to propagate along grain boundaries between 873 and 1023 K during a heating-up step of the heat treatment.
- Consecutive micropores along grain boundaries appear in the extension of the external crack tips after heat treatment.
- Oxidized bilayers form on the surfaces of external cracks.

The tensile residual stress caused by LPBF process (Figure 5a) is kept loaded to the solidification crack tips in the vicinity of the top surfaces. The preferential crack propagation perpendicular to the laser scan paths on the top surface in Figure 6d agreed well with the presence of anisotropic tensile stress with its maximum principal stress direction along laser scan direction in Figure 5. The stress concentration to the crack tip that promoted the crack initiation was calculated by Safizadeh et al. [41].

Cracking temperature range and the surface oxide layer of the crack suggest that the external crack is likely to be influenced by the two drivers, γ′ precipitation and oxidation [47, 48]. Increases in the micro-Vickers hardness after 873 and 1023 K short heat treatment (Figure 13) imply that γ′ precipitation started during heating-up process. Miao et al. [40] characterized the cracks along grain boundaries in heat-treated Inconel 738LC LPBF components and concluded that γ′ precipitation along

15272648, 2026, 18, Downloaded from https://advanced.onlinelibrary.wiley.com/doi/10.1002/adem.71079 by National Institute For, Wiley Online Library on [22/09/2026]. See the Terms and Conditions (https://onlinelibrary.wiley.com/terms-and-conditions) on Wiley Online Library for rules of use; OA articles are governed by the applicable Creative Commons License

grain boundaries promoted cracking in conjunction with the tensile residual stress originating in LPBF process. The extra stress caused by the γ′ precipitation overlaps with the strong residual stress, which leads to the initiation of the external crack during heating-up process. Considering the external crack with no oxide layer after 1023 K–0.1 h heat treatment test, the external crack seemed to be primary triggered by the γ′ precipitation.

The other driver is grain boundary oxidation. As shown by the EPMA analysis in Figure 4, crack tips were always accompanied by consecutive holes depleted in oxide-forming elements. This suggests that oxide-forming elements diffuse outward from the crack tip along grain boundaries to form oxide layers on the external crack surface, resulting in the formation of these hole chains along the grain boundaries. The residual stress opens the crack tip, and the crack then propagates inward by linking the holes along the boundaries. γ′ precipitation near the grain boundaries would be retarded compared with the surrounding matrix because γ′-forming elements near the boundaries, aluminum and titanium, are consumed by oxide formation. Micropores and γ′-deficient zones along the grain boundaries therefore promote preferential crack propagation. Repeated outward diffusion of oxide-forming elements to form consecutive holes, together with crack opening driven by residual stress, can thus lead to an external cracking.

The proposed cracking mechanism requires the combined action of preexisting cracks exposed to the surface and tensile residual stress loaded on the surface region. It implies that external cracks can be prevented by eliminating either factor. To demonstrate this crack-prevention strategy, LPBF components fabricated with scan strategy B were heat-treated after removal of the support structures by wire electric discharge machining (WEDM): these supports contained solidification cracks caused by heat accumulation. Figure 15 shows the cross-sections of the heat-treated components, confirming the effectiveness of this approach in suppressing external cracking. For practical parts manufacturing, build designs that avoid overheating and the associated solidification cracking should therefore be effective in preventing external cracks.

3.3 | Mechanism of Internal Cracking

The internal cracks originated in solidification cracks, and gas pores were found along grain boundaries, as reported in previous studies [15, 40]. Cracks initiated from these flaws and propagated along grain boundaries to form internal cracks. The local crystal strain detected in the crack edge in Figure 10 confirmed the plastic deformation caused by the crack propagation. The residual stress caused by the LPBF process and γ′ precipitation would be the driving forces behind this internal cracking. The grain boundaries in Figure 11 were characterized by the precipitation of carbide and coarse γ′. The local dissimilar microstructure caused the strain concentration, leading to the preferential crack propagation along grain boundaries.

Heat treatment at temperatures no higher than 1200 K corresponding to the temperature range 2 in Figure 8h seemed to inhibit internal crack propagation. Though the external cracking during the heating-up step would decrease the residual stress caused by LPBF process and following γ′ precipitation, the microstructure evolution, such as the disappearance of the microcellular structures and formation of chromium-rich $M_{23}C_6$ carbide during heat treatment, should also contribute to the stress release, considering the uniform crack reduction effect in specimens after heat treatment in temperature range 2 and those after 2-step heat treatment. At higher temperatures over 1200 K (range 3; Figure 8h), the higher amount of coarse γ′ precipitates should generate residual stress because of the higher negative mismatch of γ′/γ over 1073 K [49]. The compressive residual stress detected on the surface of the specimens after heat treatment at 1313 K for 2 h (Figure 5b) might have been caused by the generation of tensile stress within the components, considering the balance of internal stress. Strain-age cracking caused by the generated stress would be a principal mechanism for heat-treated specimens at temperatures over 1200 K. The lower γ′ amount at even higher temperature over 1350 K likely contributed to the crack reduction in temperature range 4 in Figure 8h, but the liquation in the grain boundaries promoted the cracking when the temperature exceeded the local solidus temperature around grain boundaries (temperature range 5; Figure 8h).

The amount of build flaws was minimized in the LPBF specimens obtained by the optimized scan strategy B. The number of internal cracks in LPBF specimens with scan strategy B did not depend on the heat treatment conditions. Internal cracks found in these specimens were mostly identified in the surface areas, so these internal cracks might be influenced by the surface oxidation discussed in the last section.

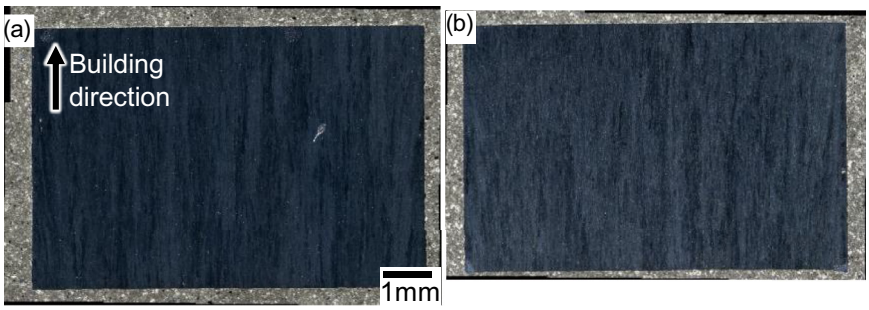


FIGURE 15 | Crack-free LPBF specimens produced using scan strategy B heat-treated after removing support structures. (a) Heat treatment at 1393 K for 2 h. (b) Heat treatment at 1393 K for 2 h followed by 1118 K for 24 h.

15272648, 2026, 18, Downloaded from https://advanced.onlinelibrary.wiley.com/doi/10.1002/adem.71079 by National Institute For, Wiley Online Library on [22/09/2026]. See the Terms and Conditions (https://onlinelibrary.wiley.com/terms-and-conditions) on Wiley Online Library for rules of use; OA articles are governed by the applicable Creative Commons License

3.4 | Heat Treatment Process Optimized for Inconel 738LC

Heat treatment for the LPBF components is generally conducted to reduce unfavorable effects such as cracking and residual stress and to engineer the microstructure for better performance. This study is mainly aimed at reducing cracks, but the influence on the microstructures should also be considered when designing the heat treatment process.

Most of the cracking sources in heat-treated specimens lie in the LPBF process that generates flaws and residual stress, resulting in the crack propagation. However, the inhibition of the crack propagation by the heat treatment at temperatures no higher than 1200 K is still beneficial to minimize the influence of the inherent build flaws. Avoiding heat treatment at higher temperatures close to solidus temperature helps to inhibit liquation cracking.

Carbide distribution along grain boundaries is also noted, considering their influences on grain growth behavior and high-temperature mechanical properties. Chromium-rich $M_{23}C_6$ carbide and titanium-rich MC carbide are formed in heat-treated Inconel 738LC LPBF components. $M_{23}C_6$ carbide and MC carbide are mutually interchangeable by the temperature range in the heat treatment. Heat treatment also influences carbide morphology by affecting the elemental distribution resulting from the precipitation and decomposition behaviors. The difference in the $M_{23}C_6$ carbide morphologies in the 1118 K–24 h heat-treated specimen and 1393 K–2 h–1118 K–24 h 2-step heat-treated one in Figure 11 is the typical example. It is presumed that the film-like $M_{23}C_6$ carbide was formed after 2-step heat treatment because of the local enrichment of chromium repelled from blocky MC carbides precipitated at higher temperatures.

Together with the function of the grain boundary carbides, the influence of trace elements such as boron and zirconium is not assessed in this study. Their influences on the high-temperature mechanical properties will be investigated in the future study to establish the proper heat treatment strategy suited for the LPBF components of nonweldable nickel-based superalloy.

4 | Conclusions

Cracks and grain boundary microstructures in heat-treated LPBF-fabricated Inconel 738LC components were characterized to clarify the mechanisms of heat treatment-induced cracking in this nonweldable nickel-based superalloy. The main findings are summarized as follows.

1. Two cracking modes, external and internal cracking, were identified in all heat-treated components.
2. External cracking initiated from the bottom or top surface of the specimens and propagated along long, straight HAGBs at 873–1023 K during the heating-up step of the heat treatment. Bilayer oxide layers on the crack surfaces and chains of micropores ahead of the crack tips along grain boundaries suggest that γ' precipitation and oxidation contribute to external cracking.
3. Internal cracking originated in the solidification cracks and gas pores along HAGBs formed during the LPBF process. Crack propagation along HAGBs depended on the heat treatment conditions. Heat treatment at 1118–1193 K was found to be effective in minimizing crack propagation.
4. LPBF process conditions optimized to minimize solidification cracking suppressed the formation of both external cracks and internal cracks originating from build flaws.

5 | Methods

5.1 | Materials and process conditions

LPBF components of Inconel 738LC nickel-based superalloy, used as a typical nonweldable precipitation-hardening heat-resistant nickel-based alloy, were investigated in this study [43]. The cylinder-shaped specimens were fabricated on a stainless-steel baseplate ($98 \times 98 \times 20$ mm) in a LPBF machine (SLM280, SLM Solutions GmbH) in the layout shown in Figure 16. Gas atomized prealloyed Inconel 738LC powder (AMPERPRINT 0151.074, Höganäs AB) was used as the powder feedstock for LPBF process. Table 1 shows the powder chemical compositions provided by the powder producer [43].

LPBF process parameters applied in this study are summarized in Table 2. The LPBF components obtained by scan strategy A contained solidification cracks in the preliminary study of this work though they contained limited amount of lack of fusion defects. Scan strategy B, characterized by the lower heat input and different scan strategy, is the optimized parameter set minimizing the solidification cracks [43]. The oxygen content in the LPBF chamber was maintained to be less than 0.01% by an argon

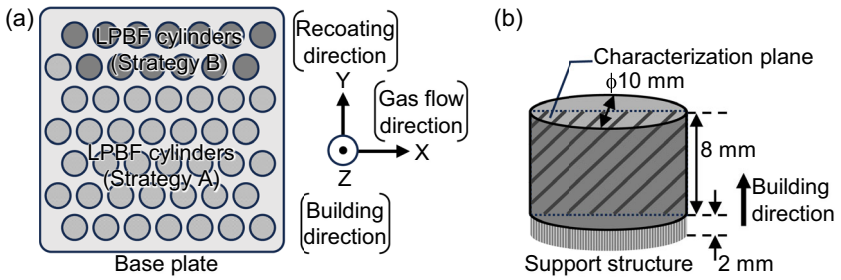


FIGURE 16 | (a) Specimen layout in the LPBF process and (b) characterizaiton section.

15272648, 2026, 18, Downloaded from https://advanced.onlinelibrary.wiley.com/doi/10.1002/adem.71079 by National Institute For, Wiley Online Library on [22/09/2026]. See the Terms and Conditions (https://onlinelibrary.wiley.com/terms-and-conditions) on Wiley Online Library for rules of use; OA articles are governed by the applicable Creative Commons License

TABLE 1 | Chemical composition of powder feedstocks [Unit: mass%].

	Ni	C	Co	Cr	Mo	W	Ta	Nb	Al	Ti
Powder	Bal.	0.10	8.5	15.9	1.7	2.5	1.8	0.88	3.5	3.5
	B	**Zr**	**Fe**	**Mn**	**Si**	**P**	**S**	**N**	**O**	
Powder	0.007	0.024	0.02	0.01	0.02	0.005	0.002	0.008	0.017	

TABLE 2 | Parameters of LPBF.

	Laser spot size, mm	Scanning strategy	Laser output, W	Scan speed, mm s^{-1}	Scan interval, mm	Layer thickness, mm	Scan rotation, deg/layer
Strategy A	0.1	Snake scan	300	1300	0.10	0.03	90
Strategy B	0.1	Snake scan	150	1000	0.05	0.03	67

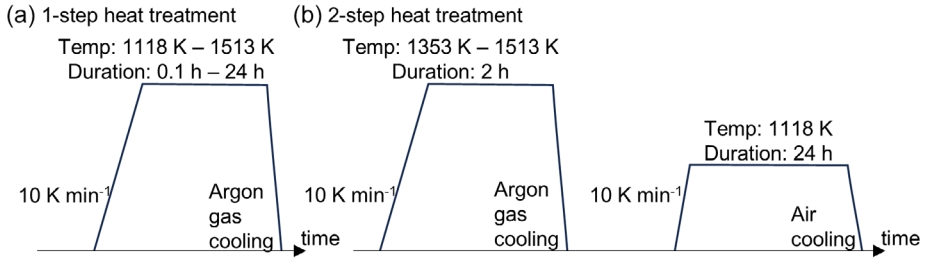


FIGURE 17 | Heat treatment program in this study, (a) 1-step heat treatment, (b) 2-step heat treatment.

gas circulating system. LPBF specimens were separated from the baseplate by WEDM.

The LPBF specimens were subjected to heat treatment according to the program shown in Figure 17. The heat treatment was performed in a small tubular furnace (FT-01VAC-50, FULL-TECH Co.) under continuous pure argon gas flow of 1.5 L min^{-1}. The specimens were cooled down to room temperature in an argon gas flow of 10 L min^{-1} to increase the cooling rate. Selected specimens were subjected to the 2-step heat treatment (Figure 17b) to simulate the standard solution-aging heat treatments for Inconel 738LC components. The second-step heat treatment was conducted in a muffle furnace, followed by the air cooling.

5.2 | Characterization Methods

Specimens were cut by the precision cutting machine in the center parallel to the building direction as shown in Figure 16b. Cut specimens were wet-polished with emery papers and finished with buff polishing using 0.06-μm colloidal silica slurry (MasterMet, Buehler). Specimens for cracks and microstructure characterization were embedded in the heat-curable resin before polishing to avoid damage to the specimen.

XRD analysis was performed using a RIGAKU FlexMini X-ray diffractometer. The sample was scanned in increments of 0.02° from 5° to 100° at a scan rate of 5° min^{-1} with a Cu-Kα X-ray source and Kβ filter. Crack morphology was characterized by a digital microscope (VHX-2000, Keyence) at a magnification of ×100. Microstructure was characterized using a SEM, (JEOL JSM-6000 LA and JSM-7200F). Elemental compositions were evaluated by EDS using an SEM equipped with an EDS detector. The crystal grain structures around cracks were characterized by an EBSD detector in JSM-7200F. The accelerating voltage and scanning step size were 20 kV and 0.25 μm, respectively. The measured data were analyzed using EDAX OIM Analysis v8 software to generate inverse pole figure (IPF), grain boundary (GB), and KAM maps. Elemental distributions, including light elements around cracks and grain boundaries, were obtained by an electron-probe microanalyzer with wavelength dispersive X-ray spectroscopy (EPMA; EPMA-8050G, Shimadzu Corp.). The signal intensities were mapped qualitatively in a grid pattern at 0.5 μm intervals with 100 × 100 μm areas at an acceleration voltage of 15 kV and a 0.2 μA current for 8 ms per point.

Hardness of the specimen was obtained using a Micro-Vickers hardness tester (AMT-7FS, Matsuzawa Co. Ltd.) with a load of 0.5 kgf for 15 s duration. The residual stresses of the as-built and heat-treated specimens on the centers of the cylinder specimens' top surfaces were obtained using an XRD residual stress measurement system (iXRD, Proto Manufacturing) after separation from the baseplate without any preprocessing. The X-ray spectrum originating from 311^{γ} diffraction peak ($2\theta = 153.1°$) obtained with the incident X-ray through 2 mm diameter point aperture from Mn-Kα X-ray tube was applied to the residual stress measurement using $\sin^2\psi$ method. Values for Young's modulus ($E = 200.6$ GPa), shear modulus ($G = 77.9$ GPa) and Poisson's ratio ($\nu = 0.28$) were taken from a standard data book [44]. The residual stress of the powder feedstock for LPBF process

15272648, 2026, 18, Downloaded from https://advanced.onlinelibrary.wiley.com/doi/10.1002/adem.71079 by National Institute For, Wiley Online Library on [22/09/2026]. See the Terms and Conditions (https://onlinelibrary.wiley.com/terms-and-conditions) on Wiley Online Library for rules of use; OA articles are governed by the applicable Creative Commons License

in a small cup was measured as a reference measurement prior to each stress measurement and it was confirmed that the obtained values fell within the range of −10 to −50 MPa. Principal stresses and maximum shear stresses were calculated from the axial residual stress along three directions using the following formula under the assumption of the plane stress condition.

$$\sigma_1 = \frac{\sigma_{0^\circ} + \sigma_{90^\circ}}{2} + \sqrt{\left(\frac{\sigma_{0^\circ} - \sigma_{90^\circ}}{2}\right)^2 + \left(\sigma_{45^\circ} - \frac{\sigma_{0^\circ} + \sigma_{90^\circ}}{2}\right)^2} \quad (1)$$

$$\sigma_2 = \frac{\sigma_{0^\circ} + \sigma_{90^\circ}}{2} - \sqrt{\left(\frac{\sigma_{0^\circ} - \sigma_{90^\circ}}{2}\right)^2 + \left(\sigma_{45^\circ} - \frac{\sigma_{0^\circ} + \sigma_{90^\circ}}{2}\right)^2} \quad (2)$$

$$\tau_{\max} = \sqrt{\left(\frac{\sigma_{0^\circ} - \sigma_{90^\circ}}{2}\right)^2 + \left(\sigma_{45^\circ} - \frac{\sigma_{0^\circ} + \sigma_{90^\circ}}{2}\right)^2} \quad (3)$$

σ_{0°: Axial stress along the laser scan direction on the specimen's top surface.

σ_{90°: Axial stress perpendicular to the laser scan direction on the specimen's top surface.

σ_{45°: Axial stress 45° to the laser scan direction on the specimen's top surface.

σ_1, σ_2: principal stresses; $\tau_{\max}$: maximum shear stress.

Author Contributions

Kosuke Kuwabara: conceptualization, methodology, investigation, data curation, writing – original draft and revised draft. **Masahiro Kusano:** resources, methodology, writing – review and editing. **Ayako Ikeda:** methodology, investigation. **Toshio Osada:** methodology, supervision, writing – review and editing. **Makoto Watanabe:** resources, supervision, project administration, fund acquisition, writing – review and editing.

Acknowledgments

This work was partly supported by a grant from the Amada Foundation (No. AF-2022201-A3).

Funding

This work was partly supported by a grant from the Amada Foundation (No. AF-2022201-A3).

Conflicts of Interest

The authors declare no conflicts of interest.

Data Availability Statement

Data will be made available upon request.

References

1. T. DebRoy, H. L. Wei, J. S. Zuback, et al., "Additive Manufacturing of Metallic Components – Process, Structure and Properties," *Progress in Materials Science* 92 (2018): 112–224, https://doi.org/10.1016/j.pmatsci.2017.10.001.

2. B. Blakey-Milner, P. Gradl, G. Snedden, et al., "Metal Additive Manufacturing in Aerospace: A Review," *Materials & Design* 209 (2021): 110008, https://doi.org/10.1016/j.matdes.2021.110008.

3. L. E. Murr, S. M. Gaytan, D. A. Ramirez, et al., "Metal Fabrication by Additive Manufacturing Using Laser and Electron Beam Melting Technologies," *Journal of Materials Science & Technology* 28 (2012): 1–14, https://doi.org/10.1016/S1005-0302(12)60016-4.

4. A. Vafadar, F. Guzzomi, A. Rassau, and K. Hayward, "Advances in Metal Additive Manufacturing: A Review of Common Processes, Industrial Applications, and Current Challenges," *Applied Sciences* 11 (2021): 1213, https://doi.org/10.3390/app11031213.

5. C. Tan, F. Weng, S. Sui, Y. Chew, and G. Bi, "Progress and Perspectives in Laser Additive Manufacturing of Key Aeroengine Materials," *International Journal of Machine Tools and Manufacture* 170 (2021): 103804, https://doi.org/10.1016/j.ijmachtools.2021.103804.

6. D. Herzog, K. Asami, C. Scholl, et al., "Design Guidelines for Laser Powder Bed Fusion in Inconel 718," *Journal of Laser Applications* 34 (2022): 012015, https://doi.org/10.2351/7.0000508.

7. H. Hyer, R. Newell, D. Matejczyk, et al., "Microstructural Development in As Built and Heat Treated IN625 Component Additively Manufactured by Laser Powder Bed Fusion," *Journal of Phase Equilibria and Diffusion* 42 (2021): 14–27, https://doi.org/10.1007/s11669-020-00855-9.

8. Y. Ro, Y. Koizumi, and H. Harada, "High Temperature Tensile Properties of a Series of Nickel-Base Superalloys on a γ/γ′ Tie Line," *Materials Science and Engineering: A* 223 (1997): 59–63, https://doi.org/10.1016/S0921-5093(96)10504-9.

9. T. Murakumo, T. Kobayashi, Y. Koizumi, and H. Harada, "Creep Behaviour of Ni-Base Single-Crystal Superalloys with Various γ′ Volume Fraction," *Acta Materialia* 52 (2004): 3737–3744, https://doi.org/10.1016/j.actamat.2004.04.028.

10. W. Xia, X. Zhao, L. Yue, and Z. Zhang, "A Review of Composition Evolution in Ni-Based Single Crystal Superalloys," *Journal of Materials Science & Technology* 44 (2020): 76–95, https://doi.org/10.1016/j.jmst.2020.01.026.

11. G. Gudivada, and A. K. Pandey, "Recent Developments in Nickel-Based Superalloys for Gas Turbine Applications: Review," *Journal of Alloys and Compounds* 963 (2023): 171128, https://doi.org/10.1016/j.jallcom.2023.171128.

12. Y. Yuan, Y. F. Gu, T. Osada, Z. H. Zhong, T. Yokokawa, and H. Harada, "A New Method to Strengthen Turbine Disc Superalloys at Service Temperatures," *Scripta Materialia* 66 (2012): 884–889, https://doi.org/10.1016/j.scriptamat.2012.01.025.

13. W. Zhang, G. Gao, X. Chen, et al., "Progress in Key Alloy Materials for Flue Gas Turbines: Alloy Design, Processing, Microstructure, and Properties," *International Journal of Minerals, Metallurgy and Materials* (2026), https://doi.org/10.1007/s12613-026-3440-7.

14. D. Grange, J. D. Bartout, B. Macquaire, and C. Colin, "Processing a Non-Weldable Nickel-Base Superalloy by Selective Laser Melting: Role of the Shape and Size of the Melt Pools on Solidification Cracking," *Materialia* 12 (2020): 100686, https://doi.org/10.1016/j.mtla.2020.100686.

15. C. Qiu, H. Chen, Q. Liu, S. Yue, and H. Wang, "On the Solidification Behaviour and Cracking Origin of a Nickel-Based Superalloy during Selective Laser Melting," *Materials Characterization* 148 (2019): 330–344, https://doi.org/10.1016/j.matchar.2018.12.032.

16. E. Chauvet, P. Kontis, E. A. Jägle, et al., "Hot cracking mechanism affecting a non-weldable Ni-based superalloy produced by selective electron Beam Melting," *Acta Materialia* 142 (2018): 82–94, https://doi.org/10.1016/j.actamat.2017.09.047.

17. Y. Lei, K. Aoyagi, K. Aota, K. Kuwabara, and A. Chiba, "Critical Factor Triggering Grain Boundary Cracking in Non-Weldable Superalloy Alloy713ELC Fabricated with Selective Electron Beam Melting," *Acta Materialia* 208 (2021): 116695, https://doi.org/10.1016/j.actamat.2021.116695.

18. X. Zhang, H. Chen, L. Xu, J. Xu, X. Ren, and X. Chen, "Cracking Mechanism and Susceptibility of Laser Melting Deposited Inconel 738

15272648, 2026, 18, Downloaded from https://advanced.onlinelibrary.wiley.com/doi/10.1002/adem.71079 by National Institute For, Wiley Online Library on [22/09/2026]. See the Terms and Conditions (https://onlinelibrary.wiley.com/terms-and-conditions) on Wiley Online Library for rules of use; OA articles are governed by the applicable Creative Commons License

Superalloy," *Materials & Design* 183 (2019): 108105, https://doi.org/10.1016/j.matdes.2019.108105.

19. N. Wang, S. Mokadem, M. Rappaz, and W. Kurz, "Solidification Cracking of Superalloy Single- and Bi-Crystals," *Acta Materialia* 52 (2004): 3173–3182, https://doi.org/10.1016/j.actamat.2004.03.047.

20. A. T. Egbewande, R. A. Buckson, and O. A. Ojo, "Analysis of Laser Beam Weldability of Inconel 738 Superalloy," *Materials Characterization* 61 (2010): 569–574, https://doi.org/10.1016/j.matchar.2010.02.016.

21. M. Taheri, "Analysis of Solidification and Liquation Cracks in the Electron Beam Welding of IN738 Superalloy," *Metallography, Microstructure, and Analysis* 10 (2021): 815–822, https://doi.org/10.1007/s13632-021-00793-z.

22. H. Kazempour-Liasi, M. Tajally, and H. Abdollah-Pour, "Effects of Pre- and Post-Weld Heat Treatment Cycles on the Liquation and Strain-Age Cracking of IN939 Superalloy," *Engineering Research Express* 1 (2019): 025026, https://doi.org/10.1088/2631-8695/ab4d6c.

23. M. Caruso and L. Frame, "Ductility Dip Cracking Mechanisms and Characterization: A Review," *Journal of Materials Science* 59 (2024): 16789–16814, https://doi.org/10.1007/s10853-024-10112-w.

24. N. J. Harrison, I. Todd, and K. Mumtaz, "Reduction of Micro-Cracking in Nickel Superalloys Processed by Selective Laser Melting: A Fundamental Alloy Design Approach," *Acta Materialia* 94 (2015): 59–68, https://doi.org/10.1016/j.actamat.2015.04.035.

25. Y. T. Tang, C. Panwisawas, J. N. Ghoussoub, et al., "Alloys-by-Design: Application to New Superalloys for Additive Manufacturing," *Acta Materialia* 202 (2021): 417–436, https://doi.org/10.1016/j.actamat.2020.09.023.

26. S. Griffiths, H. G. Tabasi, T. Ivas, et al., "Combining Alloy and Process Modification for Micro-Crack Mitigation in an Additively Manufactured Ni-Base Superalloy," *Additive Manufacturing* 36 (2020): 101443, https://doi.org/10.1016/j.addma.2020.101443.

27. W. Song, J. Yang, J. Liang, et al., "A New Approach to Design Advanced Superalloys for Additive Manufacturing," *Additive Manufacturing* 84 (2024): 104098, https://doi.org/10.1016/j.addma.2024.104098.

28. L. Zhang, Y. Li, S. Zhang, and Q. Zhang, "Selective Laser Melting of IN738 Superalloy with a Low Mn+Si Content: Effect of Energy Input on Characteristics of Molten Pool, Metallurgical Defects, Microstructures and Mechanical Properties," *Materials Science and Engineering: A* 826 (2021): 141985, https://doi.org/10.1016/j.msea.2021.141985.

29. L. N. Carter, C. Martin, P. J. Withers, and M. M. Attallah, "The Influence of the Laser Scan Strategy on Grain Structure and Cracking Behaviour in SLM Powder-Bed Fabricated Nickel Superalloy," *Journal of Alloys and Compounds* 615 (2014): 338–347, https://doi.org/10.1016/j.jallcom.2014.06.172.

30. Y. Chen, W. Wang, Y. Ou, et al., "Effect of High Preheating on the Microstructure and Mechanical Properties of High Gamma Prime Ni-Based Superalloy Manufactured by Laser Powder Bed Fusion," *Journal of Alloys and Compounds* 960 (2023): 170598, https://doi.org/10.1016/j.jallcom.2023.170598.

31. F. Zhang, L. Zhou, X. Xie, Z. Zhang, Q. Chao, and G. Fan, "Crack Inhibition and Crystallographic Texture Control in an Additively Manufactured IN738LC Ni-Based Superalloy," *Journal of Materials Research and Technology* 33 (2024): 652–666, https://doi.org/10.1016/j.jmrt.2024.09.101.

32. J. Xu, Y. Ding, Y. Gao, et al., "Improving High-Temperature Mechanical Properties of Laser Powder Bed-Fused Inconel 738 Alloy by Hot Isostatic Pressing: Tailoring Precipitates and Healing Defects," *Materials Science and Engineering: A* 862 (2023): 144285, https://doi.org/10.1016/j.msea.2022.144285.

33. A. V. Sotov, A. V. Agapovichev, V. G. Smelov, et al., "Investigation of the IN-738 Superalloy Microstructure and Mechanical Properties for the Manufacturing of Gas Turbine Engine Nozzle Guide Vane by Selective Laser Melting," *The International Journal of Advanced Manufacturing Technology* 107 (2020): 2525–2535, https://doi.org/10.1007/s00170-020-05197-x.

34. W. Zhou, Y. Tian, D. Wei, et al., "Effects of Heat Treatments on the Microstructure and Tensile Properties of IN738 Superalloy with High Carbon Content Fabricated via Laser Powder Bed Fusion," *Journal of Alloys and Compounds* 953 (2023): 170110, https://doi.org/10.1016/j.jallcom.2023.170110.

35. L. Zhang, Y. Li, Q. Zhang, and S. Zhang, "Microstructure Evolution, Phase Transformation and Mechanical Properties of IN738 Superalloy Fabricated by Selective Laser Melting under Different Heat Treatments," *Materials Science and Engineering: A* 844 (2022): 142947, https://doi.org/10.1016/j.msea.2022.142947.

36. G. Wang, L. Yang, G. Dai, et al., "Influence of Post-Heat Treatments on the Microstructure and Mechanical Properties of Inconel 738 Produced by Laser Directed Energy Deposition," *Journal of Materials Research and Technology* 33 (2024): 7182–7192, https://doi.org/10.1016/j.jmrt.2024.11.119.

37. O. Sifi, M. E. A. Djeghlal, Y. Mebdoua, S. Djeraf, and Fçal Hadj-Larbi, "The Effect of the Solution and Aging Treatments on the Microstructures and Microhardness of Nickel-Based Superalloy," *Applied Physics A* 126 (2020): 345, https://doi.org/10.1007/s00339-020-03517-2.

38. O. M. D. M. Messé, R. Muñoz-Moreno, T. Illston, S. Baker, and H. J. Stone, "Metastable Carbides and Their Impact on Recrystallisation in IN738LC Processed by Selective Laser Melting," *Additive Manufacturing* 22 (2018): 394–404, https://doi.org/10.1016/j.addma.2018.05.030.

39. J. Xu, X. Lin, Y. Zhao, et al., "HAZ Liquation Cracking Mechanism of IN-738LC Superalloy Prepared by Laser Solid Forming," *Metallurgical and Materials Transactions A* 49 (2018): 5118–5136, https://doi.org/10.1007/s11661-018-4826-6.

40. K. Miao, Z. Ding, R. Li, et al., "Mechanisms of Heat-Treatment-Induced Cracking in Additively Manufactured IN-738 Alloy" *Materials* 16 (2023): 7316, https://doi.org/10.3390/ma16237316.

41. S. Safizadeh, R. Wuthrich, and T. H. Kwok, "Stress and Crack Analysis in PBF-LB IN738 with Heat Treatment," *The International Journal of Advanced Manufacturing Technology* 139 (2025): 2073–2086, https://doi.org/10.1007/s00170-025-16016-6.

42. M. C. Rezende, L. S. Araújo, S. B. Gabriel, J. Dille, and L. H. de Almeida,et al., "Oxidation Assisted Intergranular Cracking under Loading at Dynamic Strain Aging Temperatures in Inconel 718 Superalloy" *Journal of Alloys and Compounds* 643 (2015): S256, https://doi.org/10.1016/j.jallcom.2014.12.279.

43. M. Kusano, T. Osada, and M. Watanabe, "Data-Driven Optimization of Laser Scanning Conditions in Laser Powder Bed Fusion for Defect-Free IN738LC Components," *Journal of Manufacturing Processes* 151 (2025): 354–371, https://doi.org/10.1016/j.jmapro.2025.07.023.

44. Nickel Institute, Alloy IN-738 Technical Data: A Practical Guide to the Use of Nickel-Containing Alloys No. 497 (Nickel Institute, 2020), Accessed July 23, 2025, https://nickelinstitute.org/media/4690/ni_inco_497_alloy738.pdf.

45. J. H. Boswell, D. Clark, W. Li, and M. M. Attallah, "Cracking during Thermal Post-Processing of Laser Powder Bed Fabricated CM247LC Ni-Superalloy," *Materials and Design* 174 (2019): 107793, https://doi.org/10.1016/j.matdes.2019.107793.

46. M. Bartošák, V. Mára, and I. Šulák, "Effects of Temperature and Strain Rate on Isothermal Low-Cycle Fatigue Behaviour of Inconel 718 Superalloy: Damage Mechanisms, Microstructure Evolution, and Life Prediction," *International Journal of Fatigue* 198 (2025): 109005, https://doi.org/10.1016/j.ijfatigue.2025.109005.

47. S. Chandra, N. Paulose, and R. K. Rai, "The Coupling Effects of Oxidation and Temperature on the Low Cycle Fatigue Deformation

15272648, 2026, 18, Downloaded from https://advanced.onlinelibrary.wiley.com/doi/10.1002/adem.71079 by National Institute For, Wiley Online Library on [22/09/2026]. See the Terms and Conditions (https://onlinelibrary.wiley.com/terms-and-conditions) on Wiley Online Library for rules of use; OA articles are governed by the applicable Creative Commons License

Behavior of CM 247 DS LC Alloy," *International Journal of Fatigue* 194 (2025): 108858, https://doi.org/10.1016/j.ijfatigue.2025.108858.

48. P. Strunz, M. Petrenec, V. Davydov, J. Polák, and Přemysl Beran, "Misfit in Inconel-Type Superalloy," *Advanced Materials Science and Engineering*2013 (2013): 1, https://doi.org/10.1155/2013/408347.

49. C. A. Schneider, W. S. Rasband, and K. W. Eliceiri, "NIH Image to ImageJ: 25 Years of Image Analysis," *Nature Methods* 9 (2012): 671–675, https://doi.org/10.1038/nmeth.2089.

Supporting Information

Additional supporting information can be found online in the Supporting Information section.

15272648, 2026, 18, Downloaded from https://advanced.onlinelibrary.wiley.com/doi/10.1002/adem.71079 by National Institute For, Wiley Online Library on [22/09/2026]. See the Terms and Conditions (https://onlinelibrary.wiley.com/terms-and-conditions) on Wiley Online Library for rules of use; OA articles are governed by the applicable Creative Commons License